Vacuum 184 (2021) 109914

Contents lists available at ScienceDirect

Vacuum

journal homepage: http://www.elsevier.com/locate/vacuum

Surface microstructure and property modifications in AISI 304 stainless steel induced by pseudospark pulsed electron beam treatments

Xiaotong Cao, Jing Hu *, Weijie Huo, Xuecheng Xi, Wansheng Zhao

School of Mechanical Engineering, Shanghai Jiao Tong University, NO.800 Dongchuan Road, Shanghai, 200240, China

ARTICLE INFO

Keywords:
Pseudospark pulsed electron beam (PSPEB)
AISI 304 austenite stainless steel
Surface modification
Homogenous submicron grain modified layer
Multiple abundant plastic deformation microstructures
Corrosion resistance

ABSTRACT

In this paper, the modifications of microstructure, mechanical properties and corrosion behaviors of AISI 304 austenite stainless steel treated by pseudospark pulsed electron beam (PSPEB) with different number of pulses were investigated. PSPEB is a high frequency superfine pulsed electron beam characterized by the rapid current growth of~10^{12} A/s, high power density of~10^{9} W/cm^2, short-duration pulse of10^{2}~10^{3} *ns* and self-focusing beam diameter of0.5~6 mm. The results of EDS analysis indicated that the precipitated ferrite phase dissolved into the matrix, forming the homogenous composition in the modified layer. Microstructure observations revealed that the homogenous submicron grains with slip bands in different directions were distributed fully in the modified layer completely replacing the original coarse grains (more than 10 μm) after 5000 pulses PSPEB treatment. Simultaneously, the multiple abundant microstructures including dislocations, sub-boundaries and nanotwins with the twin lamella thickness no more than 8 nm were induced into the modified layer. The microhardness of AISI 304 stainless steel was increased with the number of PSPEB pulses, which was mainly attributed to the grain refinement and plastic deformation strengthening in the modified layer. Potentiodynamic polarization and electrochemical impendence spectrometry (EIS) tests of AISI 304 stainless steel before and after PSPEB treatment in the 5 wt% NaCl solution showed that the 5000 pulses treated specimen exhibited the highest corrosion potential and polarization resistance due to the homogeneous alloying element distribution in the modified layer.

1. Introduction

AISI 304 austenite stainless steel is a significant class of stainless steel due to its outstanding properties, such as superior strength, ductility [1] and reasonable corrosion resistance [2], which are favorable for a wide range of industrial and medical applications [3,4]. However, the wear resistance of AISI 304 stainless steel is reasonably poor due to its low hardness as compared to tool steel [5,6]. In addition, it is well known that AISI 304 stainless steel is extremely susceptible to pitting corrosion in the solution containing halogen ions, especially chloride ions. Hong and Nagumo [7] investigated the effect of chloride concentration on early stages of pitting for AISI 304 stainless steel by ac impedance method, revealing that there was a required minimum chloride concentration above which the pitting on the surface can be activated into metastable propagation. Currently, number of research works are focused on the changes in surface microstructure of AISI 304 stainless steel to improve theses defects. Chen [8] obtained that the generation of nanotwins and nanograins near the surface was capable of promoting the hardness and yield strength of AISI 304 stainless steel. Moayed [9] investigated the effect of grain size on pitting corrosion of AISI 304L austenitic stainless steel, demonstrating that the frequency of metastable pitting initiation was decreased with grain refinement.

In the past decades, the electron beam treatment technology has been rapidly developed as an efficient surface modification technique to alter the microstructures and improve the properties of AISI 304 austenite stainless steel surface. As demonstrated in the investigation of microstructures and corrosion mechanism of AISI 304 stainless steel irradiation by high current pulsed electron beam, the multiple abundant microstructures including dislocations, stacking fault, twin planar and supersaturated vacancies were formed within the irradiated surface, which promoted the formation of a thick passive layer and delayed the corrosion process [10]. Proskurovsky et al. [11] investigated the low-energy high-current electron beam technology for surface modification of metallic material, showing that a fast crystallization of the liquid phase made the matrix phase grains become much smaller and a submicron (≈ 0.5 μm) structure was formed on steel AISI 304 surface

* Corresponding author.
E-mail address: jhgdb@sjtu.edu.cn (J. Hu).

https://doi.org/10.1016/j.vacuum.2020.109914
Received 3 September 2020; Received in revised form 9 November 2020; Accepted 10 November 2020
Available online 17 November 2020

after the electron beam irradiation, which reduced the tendency to pitting corrosion. Compared with other conventional surface treatment techniques, electron beam is a particularly superior technique due to its extremely heating and cooling rates (10^6~10^9 K/s) induced by the electron beam energy deposition near the surface of metallic materials within a few microns [12,13]. As a result of microstructure modification, phase change, and grain refinement in the surface layer, the hardness and corrosion resistance can be significantly improved after the treatment [14–16].

However, the existing electron beams used for surface treatment technique are mainly high-current pulsed electron beam (HCPEB) and continuous electron beam, both of which have their limitations. The former electron beam is characterized by the low pulse frequency (0.1~0.3 Hz) and large beam spot diameter (40~60 mm), which is limited to deal with fine geometric dimension parts, especially complex parts or parts with gaps, slants and inflection points [17,18]. Okada et al. [18] investigated surface polishing of metal mold with large-area electron beam irradiation, showing that the roughness of the irradiated surface was increased with the tilting angle, and the effect of the surface treatment by large-area electron beam was reduced. The combination of the low frequency and large beam spot diameter also makes HCPEB difficult to be used as a scanning electron beam. The continuous electron beam is characterized by the high accelerate voltage (50~60 kV) and focused beam spot diameter (0.1~6 mm), usually acting as a scanning electron beam source. However, compared with pulsed electron beam treatment, this high accelerate voltage combined with continuous energy input on the sample surface normally caused longer insulation time and lower cooling rate on the surface, resulting in grains coarsening [19]. In addition, in the pulsed electron beam treatment process, only a thin surface layer (10 μm) was affected, without impact on the base metal while the modified layer after the continuous electron beam treatment was increased to ~100 μm [20,21]. Thus, compared with the current popular electron beam source, the pseudospark pulsed electron beam (PSPEB) characterized by the rapid current growth of~10^{12} A/ s, short pulse duration of10~10^3 *ns*, wide-range pulse frequency of 1~3000 Hz, high power density of~10^9 W/cm^2 and self-focusing beam diameter of0.1~5mm is a better selection for material surface treatment [22–25]. These unique properties are favorable for processing the surface in a high frequency scanning manner. The Gaussian energy distribution characteristic of PSPEB in the radial direction caused the electron beam energy mainly concentrated in a small area of the beam spot center, which promoted the processing efficiency and energy transportation on a micro-scale processing surface area [26]. Additionally, the rapid current growth and high-power density of PSPEB are capable of facilitating the formation of submicron and nanocrystalline grains in the processed layer due to the fast heating and cooling rates.

In this work, a surface treatment technique by PSPEB characterized by the small diameter and high frequency properties is presented, and its effects on a diversity of properties of the surface layer of AISI 304 austenite stainless steel are investigated experimentally. This paper is organized into the following sections: In *Sec*II, the experimental setup and procedures are presented, including sample preparation, a detailed description of PSPEB device, and measuring methods of the material properties. In section III, the modification results of microstructure and properties of the samples treated by PSPEB are presented, and the mechanism of microstructure evolution is discussed. The conclusions are summarized in Sec IV.

2. Experimental setup and procedures

2.1. Sample preparation

The chemical compositions of the workpiece material of AISI 304 austenite stainless steel are shown in Table .1. Prior to PSPEB treatment, all samples were cut into cuboids with dimension of20 mm × 20 mm × 3 mm. Then, each sample was properly grounded with sandpapers and polished with 0.5 μm diamond paste to produce a mirror-like surface without scratches.

Table 1
The chemical compositions of the AISI 304 stainless steel (wt%).

Cr	Ni	Si	Mo	C	Fe
18.0–20.0	8.0–11.0	1.00	2.00	0.08	Balance

2.2. PSPEB treatment

The schematic diagram of PSPEB treatment facility is illustrated in Fig. 1, including a pseudospark discharge chamber, high-voltage pulse network, vacuum chamber, two-stage vacuum pumping system and DAQ workbench. The pseudospark discharge chamber consists of hollow cathode, anode, and multiple copper inter-gaps as the PSPEB source for material treatment. In the center of the hollow cathode and anode, there is a common aperture with 3 mm diameter. The insulation material is teflon. The hollow cathode is connected to the high voltage power supply via a 20 MΩ current-limiting resistor. The pressure range of the presented experimental work is within4~8 × 10^{-1} Pa. The current and voltage waveforms of PSPEB are shown in Fig. 2, and the electron beam is operated under 22.5 kV acceleration voltage and 200 A beam current. The interval time between each pulse is 0.2 s. The primary operating parameters are presented in Table 2:

2.3. Characterization techniques

In this work, the phase composition of the surface layer was examined by X-ray diffraction (XRD, Bruker Advance D8 with Cu-Kα). The microstructure and element distribution were observed by a field emission scanning electron microscope (SEM, JSM-7800F) and a time of flight secondary ion mass spectrometry (TOF-SIMS, GAIA3 Model 2016). Before microstructure observations, cross-section of samples was etched in aqua regia alcohol solution. The grain structure examination was performed by electron backscattered diffraction (EBSD, Aztec Nordlys Max3). The more details about microstructure in the modified layer were investigated using a Talos F2000X G2 transmission electron microscope (TEM). The specimen for TEM observation was prepared by focus ion beam (FIB) cutting with thickness of ~10 nm.

The surface microhardness was measured using HV-1000 micro Vickers. The electrochemical measurements were implemented in a standard three-electrode cell in 5 wt% NaCl solution via a CHI660D electrochemical workstation, which had a Pt counter electrode and a saturated calomel electrode (SCE). All samples were soaked in 5 wt% NaCl water solution for 30 min to guarantee that the open circuit

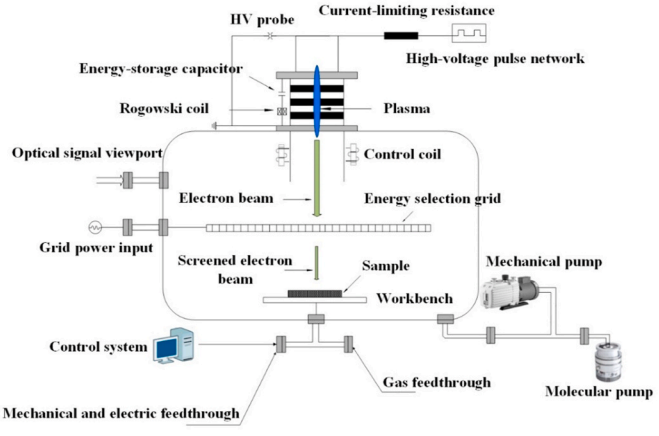

Fig. 1. Schematic diagram of PSPEB discharge device.

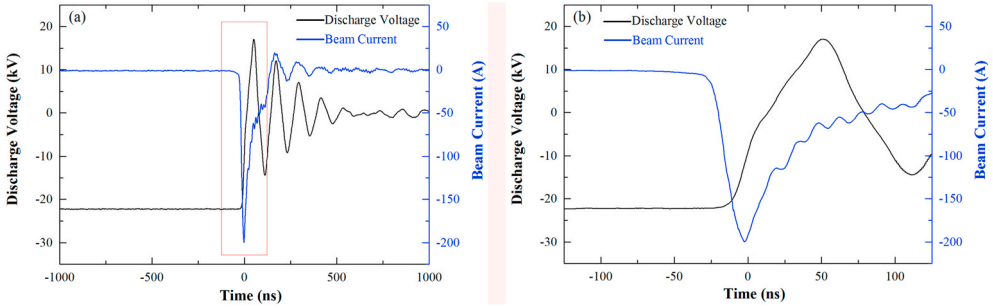

Fig. 2. Current and voltage waveforms of PSPEB: (a) whole waveform; (b) partial enlarged waveform.

Table 2
Parameters of PSPEB process.

Parameters	Values
Acceleration voltage	22.5 kV
Current	200 A
Frequency	5 Hz
Beam spot diameter	3 mm
Pulse duration	100 ns
Pulse count	50, 500, 5000

potential was maintained stable for all tests. The area exposed to the NaCl water solution was $1cm^2$ for the convenience of measurements, including the irradiation area and the coated non-irradiation area. Before immersed into the solution, the non-irradiated area is coated with enamel to prevent the electrochemical measurement of the irradiated area from being affected, and the area set aside for testing is about $7.5mm^2$, which is mainly the irradiation area. During all the presented experiments and tests, the temperature of the solution was kept at the room temperature. Potentiodynamic polarization curves were determined with a scanning rate of5 mVS^{-1}, and scanning range of cathodic polarization was set from −0.6 V to −0.1 V (SCE). The electrochemical impedance spectroscopy (EIS) measurements were recorded at the open circuit potential in the frequency range from 10^{-1} Hz to10^5 Hz, with a sinusoidal actuating signal of perturbation of 10 mV.

3. Results and discussions

3.1. Microstructure modifications analysis

3.1.1. Surface micromorphology analysis

The micromorphology of modified areas on the AISI 304 stainless steel sample surfaces after PSPEB treatment with 50, 500, and 5000 pulses are investigated by SEM and displayed in Fig. 3. As shown in Fig. 3(a) and (b), the craters are formed on the 50 pulses treated surface with two kinds of micromorphology. One kind of craters are randomly dispersed on the surface with smaller diameter less than 5 μm, and another kind of craters are clustered together with larger diameter (10 μm). According to the results presented in Refs. [27–29], the crater is formed following local melting and eruption, preferentially in the locations with inclusions (many carbon-containing inclusions randomly distributed on the surface in this work) and alloying element precipitated secondary phase (ferrite secondary phase with Cr element segregation distributed on the austenite grain boundaries in this work) due to the relative lower melting point, or structural defect surrounded by non-equilibrium thermal stress reinforcement. Clusters of craters with bottom and bulge are caused by multiple eruptions at adjacent positions. With the number of pulses increased to 500 (Fig. 3(c) and (d)), the connected bulges and depressions arise, while the eruption micromorphology becomes less conspicuous. The increase of the pulse number causes multiple eruptions at the same location, thus forming the fold micromorphology with the connected bulge and depression. Fig. 3(e) and (f) displays the surface micromorphology after 5000 pulses

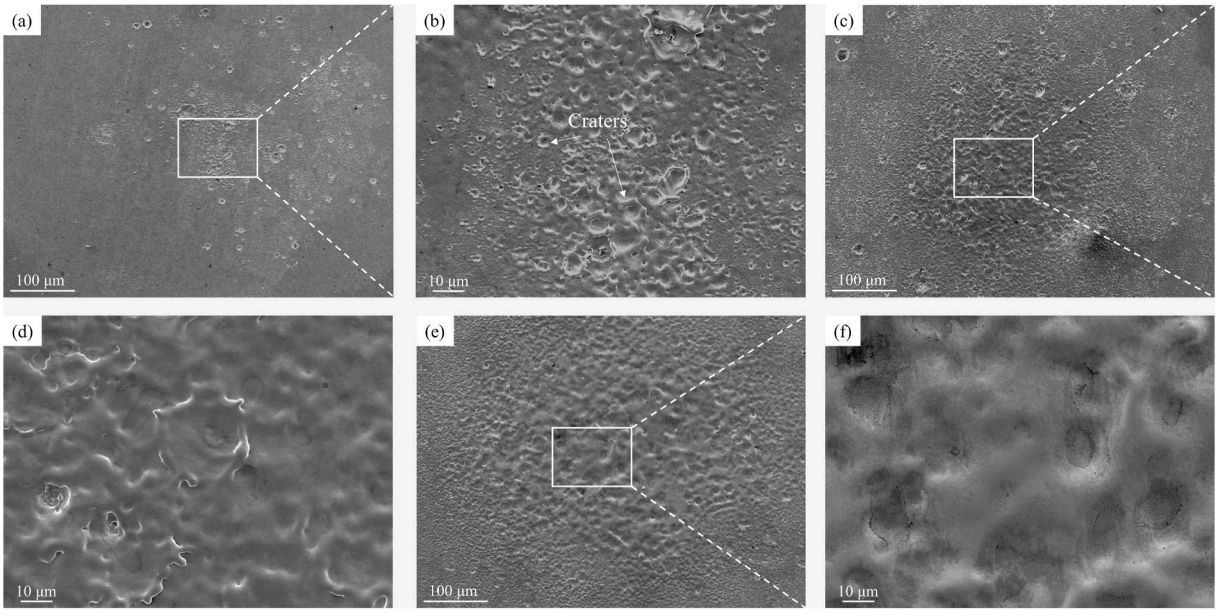

Fig. 3. SEM images of AISI 304 stainless steel sample surfaces after PSPEB treatment of: (a–b) 50 pulses; (c–d) 500 pulses; (e–f) 5000 pulses.

treatment, and the height difference between the bulge and depression is greater compared with 500 pulses. The continuous melting and eruption of the carbon-containing inclusion particles and precipitated ferrite secondary phase with Cr element segregation significantly reduce the concentration in the outer surface layer, while those in the deeper layer become the preferred locations for eruption as shown in paper [30]. The deeper eruption results in the increase of the height difference between the bulge and depression.

3.1.2. Phase analysis

The phase variation of the AISI 304 stainless steel samples before and after PSPEB treatment under varying beam pulses are detected and the results are illustrated in Fig. 4. The XRD pattern in Fig. 4(a) shows that the untreated sample surface is composed of abundant austenite phase and little ferrite phase. According to the standard pdf card #52–0513, the (111) plane is the preferred orientation of AISI 304 austenite stainless steel. The preferred orientation of samples before and after PSPEB treatment with 50 and 5000 pulses are all reserved, while the ferrite phase is disappeared after 5000 pulses treatment, which undergoes substantial break-up and dissolution in the local melting and eruption processes [31]. Furthermore, the full widths at half maximum (FWHM) of diffraction peaks for austenite (111), (200) and (220) planes are increased with the number of pulses, indicating that the austenite grain undergoes refinement after PSPEB treatment, and the similar results are also presented in Ref. [32,33]. The specific numerical relationship between FWHM of diffraction peak for austenite phase and pulse number is shown in Fig. 4(b). The FWHM of the (111) diffraction peak is increased from 0.203° to 0.67° after 5000 pulses treatment, which is approximately triple the FWHM of untreated sample, while the FWHMs of the (200) and (220) diffraction peaks are both double the FWHM of untreated sample, indicating that PSPEB surface treatment with 5000 pulses has a great effect on the austenite grain refinement. The increase in the pulse number means that the surface will undergo a more cycles of rapid heating and cooling processes, resulting in more and more crystal nuclei, which have no enough time to grow up. Thus, the grain refinement becomes more obvious with the increase of pulse number, which is identical with the results obtained in paper [34].

3.1.3. Surface element distribution analysis

Fig. 5 presents the distribution of segregation alloying element of AISI 304 stainless steel sample surfaces before and after PSPEB treatment. Fig. 5(a) is a typical SEM image of the untreated sample, showing the curved ferrite precipitating on the boundary of the equiaxial austenite grain. TOF-SIMS result of Cr element distribution on the untreated sample surface are displayed in Fig. 5(b). The color variation from dark blue to deep red corresponds to the increase of Cr element content. As shown in Fig. 5(b), the Cr element distribution at ferrite phase presents blue-green color, which is different from the austenite in dark blue, indicating the formation of Cr element segregation here. Refer to the 5000 pulses treated sample as shown in Fig. 5(c), the curved precipitated phase on the grain boundary are removed. Moreover, TOF-SIMS result given in Fig. 5(d) reveals that the Cr element distribution map of the whole surface shows dark blue without significant color variation, indicating the disappearance of the Cr element segregation and the formation of homogenous structure on the 5000 pulses treated surface, which is identical with the XRD result that the ferrite phase is disappeared after 5000 pulses treatment.

Compared with the TOF-SIMS result of the untreated sample, the distribution of Cr alloying element under 5000 pulses PSPEB treatment is more homogenous, which is identical with the result in Ref. [35]. In the PSPEB surface treatment process, the precipitated ferrite secondary phase with Cr alloying element segregation is the preferred location for melting, which promotes the eruption of the precipitates and formation of smaller parts, resulting in the segregated Cr alloying element redistributed in the vicinity of the craters over a larger zone than the size of the initial precipitates. With sufficient and intensive PSPEB pulses, the break-up of the ferrite secondary phase precipitate and its subsequent dissolution greatly reduce the level of Cr element segregation, forming the homogenous composition in the modified layer [31,36].

3.1.4. Surface and cross section microstructure analysis

Fig. 6 gives the evolution of microstructure on the AISI 304 stainless steel sample surfaces after PSPEB treatment with 50, 500, and 5000 pulses. As shown in Fig. 6(a) and (b), the original coarse grains (more than 10 μm) and a small number of submicron grains (500 nm, marked as white arrows) both appear on the 50 pulses treated surface. Simultaneously, some slip bands (marked as yellow arrows) are also formed on the surface. With the number of pulses increased, the slip bands and submicron grains are both enhanced (Fig. 6 (c)–(f)), illustrating a greater plastic deformation amount and grain refinement effect. After 5000 pulses, the homogenous submicron grains are distributed fully on the modified surface completely replacing the coarse grains as displayed in Fig. 6(e). The rapid heating process of PSPEB treatment, which has a pulse rise time with ~10 ns [37], induces a high degree of superheat on the sample surface, forming many crystallization nuclei [38]. Moreover, the pulse duration is only 100 ns and the cooling rate is very fast, so that the crystallization nuclei have not enough time to grow up, resulting in the formation of submicron grains on the treated sample surface. On the high magnification image of Fig. 6(f), many slip bands in different directions become wider and longer compared with the 500 pulses treated sample, illustrating that greater plastic deformation amount has occurred after 5000 pulses treatment. Besides, the twins are also observed in some submicron grains (marked with yellow circle). There is usually more than one twin boundary in a submicron grain and the twin

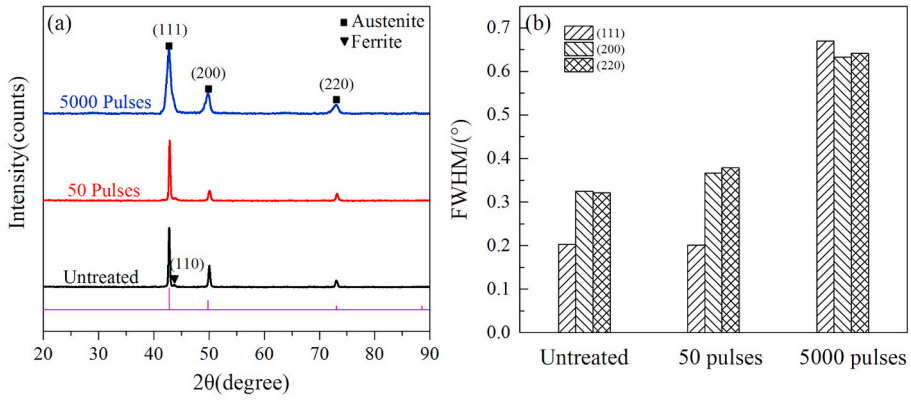

Fig. 4. XRD analysis of AISI 304 stainless steel samples before and after PSPEB treatment with 50 and 5000 pulses: (a) XRD pattern; (b) the variation in the full width at half maximum (FWHM) of diffraction peak for austenite phase with pulse number.

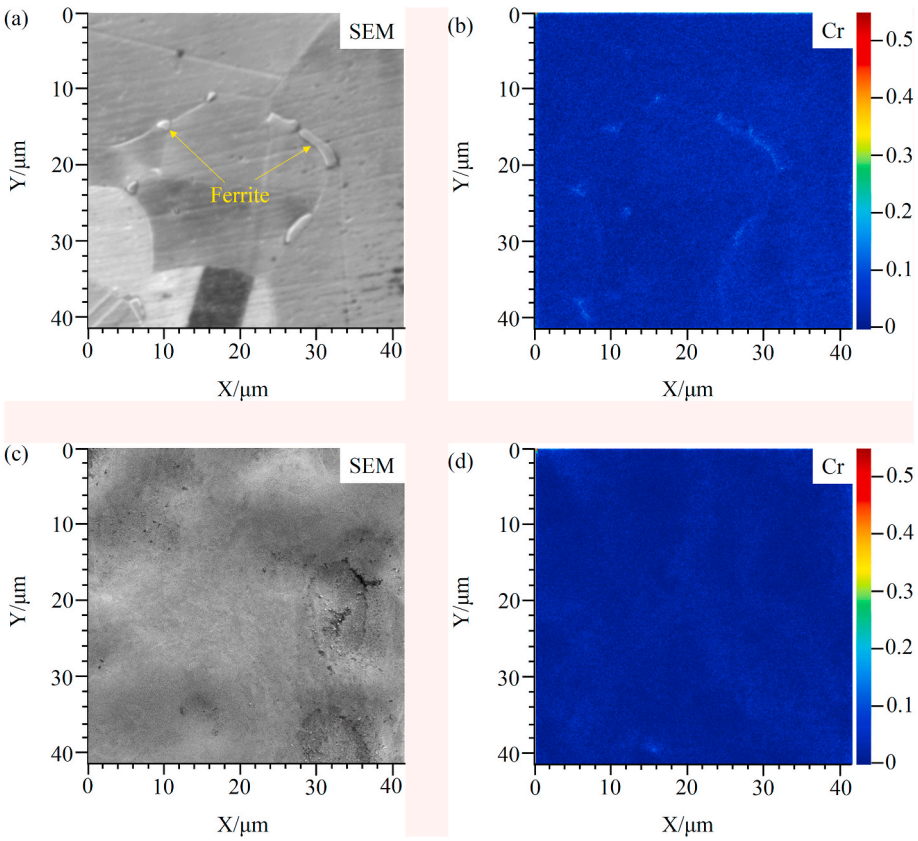

Fig. 5. SEM images and TOF-SIMS results of AISI 304 stainless steel sample surfaces before and after PSPEB treatment: (a) SEM image and (b) TOF-SIMS result of Cr element distribution on the untreated sample surface; (c) SEM image and (d) TOF-SIMS result of Cr element distribution on 5000 pulses treated sample surface.

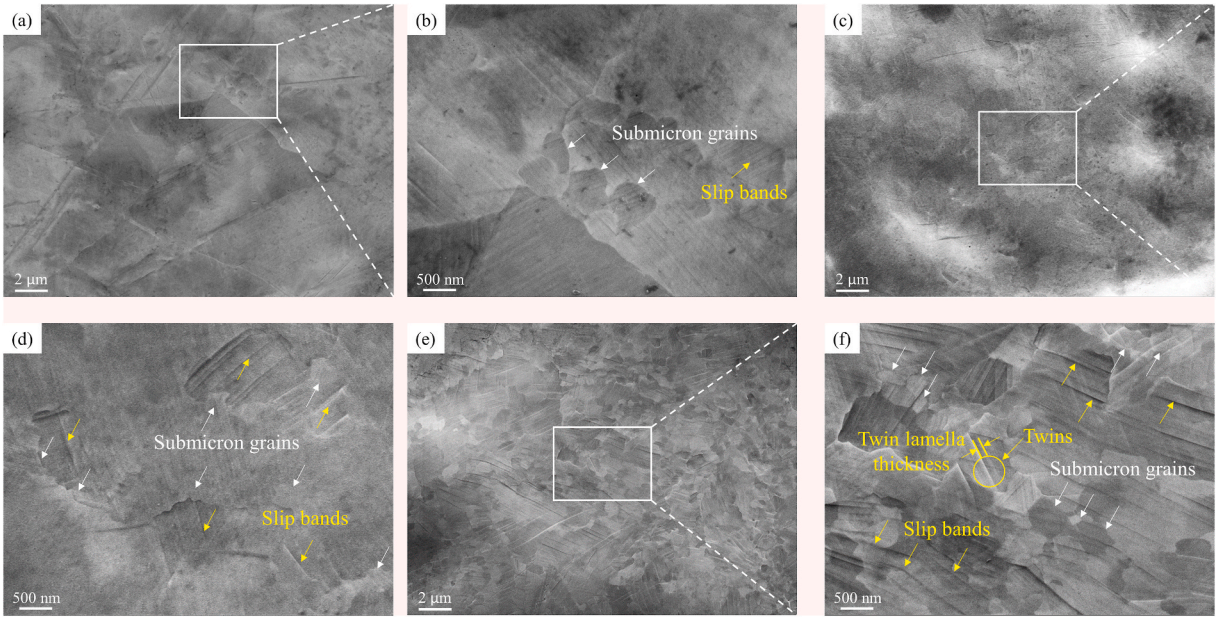

Fig. 6. SEM images of AISI 304 stainless steel sample surfaces after PSPEB treatment of: (a–b) 50 pulses; (c–d) 500 pulses; (e–f) 5000 pulses.

lamella thickness varies within 10~10^2 nm, revealing the formation of submicron twins and nanotwins in the modified surface after 5000 pulses treatment. The appearance of the slip bands and twins is related to the plastic deformation in the cooling recrystallization process [39].

Fig. 7 shows the evolution of microstructure on the AISI 304 stainless steel sample cross sections after PSPEB treatment with 50 and 5000 pulses. PSPEB technique allows high energy deposition within narrow depths near the material surface in a short time, forming the modified layer of a few microns and the beneath transition zone of tens microns. There is a clear dividing line between the modified layer and the transition zone on the cross section after treatment. The dense microstructures with unclear grain boundaries are formed in the modified layer,

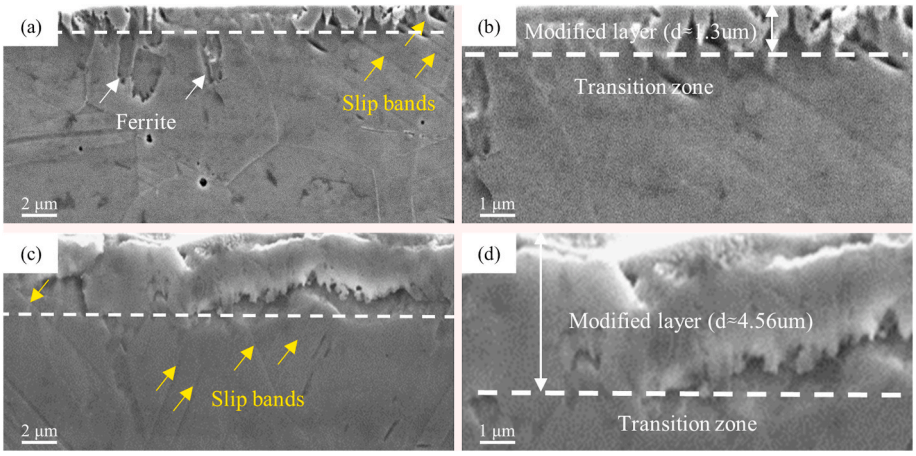

Fig. 7. SEM images of cross-sections of etched AISI 304 stainless steel samples after treatment: (a–b) 50 pulses; (c–d) 5000 pulses.

while the grains of the transition zone are relatively coarse as illustrated in Fig. 7(a) and (c). Ferrite phase are only appeared on the 50 pulses modified layer, consistent with the XRD result in Fig. 4. In addition, the slip bands are observed in both the modified layer and transition zone as marked with yellow arrows in Fig. 7(a) and (c). The thickness of the modified layer is increased from 1.3 μm under 50 pulses treatment to 4.56 μm under 5000 pulses treatment, with the homogeneity of the modified layer improved as shown in Fig. 7(b) and (d). This increase in thickness is due to the effect of heat accumulation in the underlying substrate material with short interval pulse electron beam [40,41].

The EBSD patterns present the grain properties on the cross-section of modified layer after PSPEB treatment with 5000 pulses in Fig. 8(a)-(c). The step for acquiring maps is 30 nm. Fig. 8(a) shows the band contrast map, which is capable of illustrating the grain size and grain boundary of the cross-section. Most of the grains are less than 1 μm in diameter, while a few grains over 1 μm have many sub-boundaries distributed within that (marked as white arrows). The boundary of grains is largely curved undergoing deformation. Fig. 8(b) gives the IPF-Z map of the cross-section of sample under 5000 pulses treatment. It is found that the grains exhibit random orientations. Furthermore, the statistic distribution of grain diameter for austenite phase of the cross-section of sample under 5000 pulses treatment is shown in Fig. 8(c). As illustrated in the graph, the percentage of the austenite grains less than 1 μm in diameter is approximate 97.7%, and the proportion of grains within 50~100 nm is the largest. Compared with the grain diameter of the untreated sample with most over 10 μm, the surface treatment of AISI 304 stainless steel sample by PSPEB results in a great grain refinement in the modified layer.

The TEM technique is adopoted to further investigate the fine microstructures in the modified layer in detail. Fig. 9 displays the bright field TEM images corresponding to the cross-section of modified layer of 5000 pulses sample. Fig. 9(a) is the total micrograph of modified layer, and displays the microstructures such as twins (marked as red squares), dislocations (marked as yellow squares) and sub-boundaries (marked as blue squares). Fig. 9(b) and (c) show the high magnification images of the twins marked with “A” and “B” respectively in (a). Five continous nanotwins with the thickness of the twin lamella no more than 8 nm are formed in the modified layer as shown in Fig. 9(b), illustrating that considerable plastic deformation has occurred. Moreover, the nanotwins appear at the localtion of dislocation tangle and are increased with that tangle as presented in Fig. 9(c), revealing that the dislocations with concentrated stress tend to become the uncleation point of twins. Fig. 9 (d) and (e) show the high magnification images of the dislacation tangle and dislacation cells marked with “C” and “D” respectively in (a). After 5000 PSPEB pulses treatment, the dislocations are formed in the modified layer, and the density of the dislocations in some regions is extremely high, almost filling the entire grian, forming dislocation cells, which proves the existence of large amout of plastic deformation in the modified layer. The similar results are also obtained in paper [42]. Fig. 9 (f) shows the high magnification micrograph of the zone marked with “E” in (a). The sub-boundaries and submicron grains both appear in a larger grain, illustrating that a relatively large grain undergoes

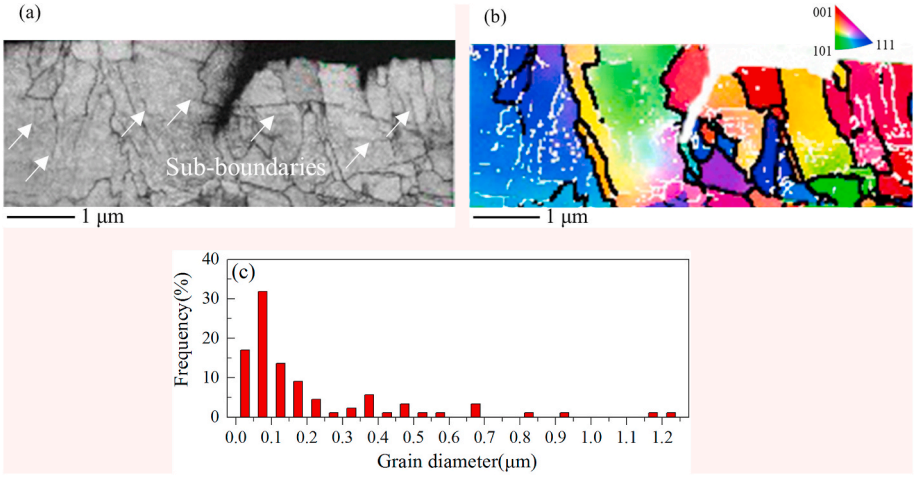

Fig. 8. EBSD maps on cross-section of modified layer of AISI 304 stainless steel sample after 5000 pulses treatment: (a) band contrast map; (b) IPF-Z map; (c) grain diameter distribution map.

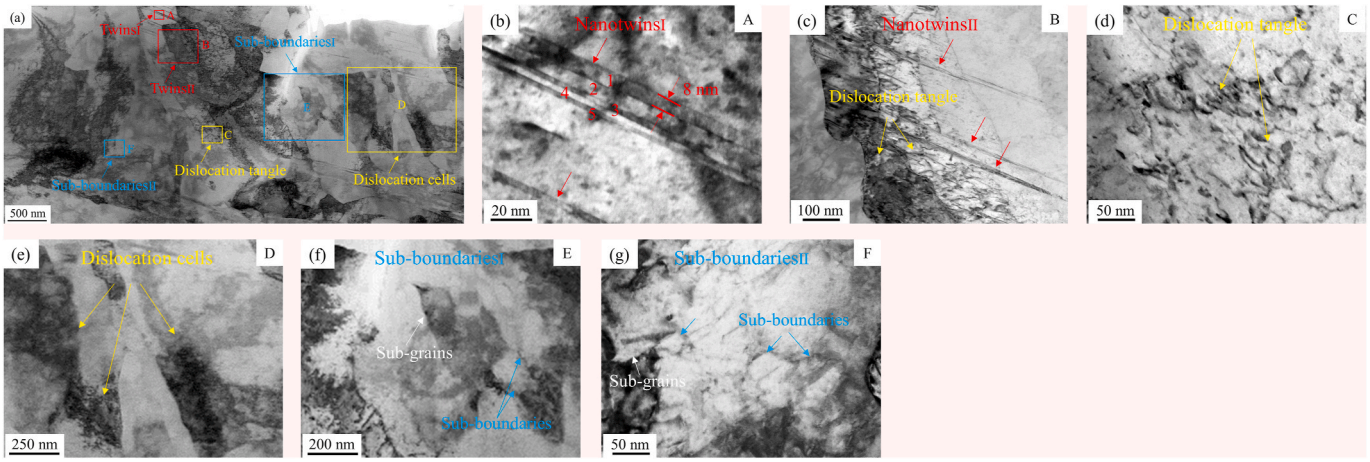

Fig. 9. Bright field TEM images on cross-section of modified layer of AISI 304 stainless steel sample after 5000 pulses treatment: (a) the total micrograph of modified layer; (b) the high magnification image of the twinsIzone marked with "A" in (a); (c) the high magnification image of the twins IIzone marked with "B" in (a); (d) the high magnification image of the dislocation tangle zone marked with "C" in (a); (e) the high magnification image of the dislocation cells zone marked with "D" in (a); (f) the high magnification image of the sub-boundariesIzone marked with "E" in (a); (g) the high magnification image of the sub-boundaries IIzone marked with "F" in (a).

dislocation deformation to form sub-boundaris, which then develop into sub-grains with a smallar diameter. The similar result is capable of being obtained in Fig. 9(g), which shows the high magnification micrograph of the zone marked with "F" in (a), while the formed sub-grains are nanocrystals.

Fig. 10 gives the SEAD parttens for different regions and the HRTEM images on cross-section of modified layer of AISI 304 stainless steel sample after 5000 pulses PSPEB treatment. Fig. 10(a) and (b) show the bright field image and its corresponding SAED partten marked with yellow arrow in (a). The index of the SAED partten of zone A given in Fig. 10(b) confirms the austenite lattice, and the orientation of the crystal plane is consistent with the XRD test result in Fig. 4. Fig. 10(c) and (d) present the bright field image and its corresponding SAED partten marked with yellow circle in (c). It is found that the diffraction spots are symmetrically distributed along the {111} plane by the yellow solid frame and red dashed frame as shown in Fig. 10(d), forming a typical twin orientation relationship, which proves the formation of twins in the modified layer and consistent with the result in Fig. 9. From

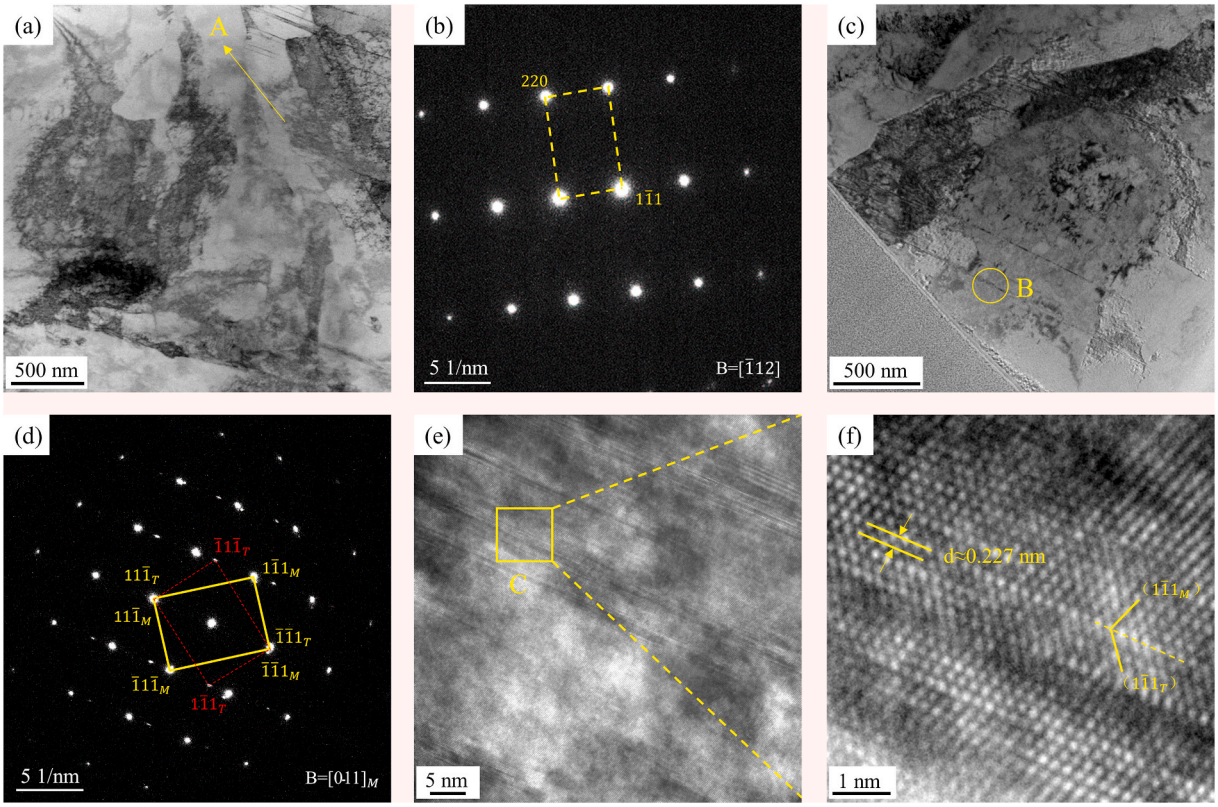

Fig. 10. TEM images on cross-section of modified layer of AISI 304 stainless steel sample after 5000 pulses treatment: (a–b) Bright field image and its corresponding SAED pattern marked with yellow arrow in (a); (c–d) Bright field image and its corresponding SAED pattern marked with yellow circle in (c); (e–f) HRTEM images of (c). (For interpretation of the references to color in this figure legend, the reader is referred to the Web version of this article.)

the HRTEM images of the twins Fig. 10(e) and (f), the interplanar crystal spacing is approximately 0.227 nm, which is greater than the standard vaule, indicating the formation of tensile stress in the modified layer.

3.1.5. Discussion on the mechanism of microstructure evolution

Pseudospark pulsed electron beam (PSPEB) surface treatment is a rapid heating and cooling treatment technology, which is characterized by the very short rise and duration time. In this surface treatment process, the rapid heating rate induces a high degree of superheat. After that, during the cooling and recrystallization process, an amount of nuclei are formed but there is no enough time for them to grow up due to the high cooling rate. Thus the crystallization nucleation rate is promoted and the grain growth time is reduced, resulting in a greatly grain refinement.

Furthermore, the surface of the sample is rapidly and repetitively heating and cooling with more cycles by the increase of the pulse number, which is greatly favorable for the crystal nucleation and grain refinement processes. As shown in Fig. 6, the submicron grains are obviously increased with the number of pulses. The submicron grains are homogenously distributed on the modified surface, and completely replace the original coarse grains after 5000 pulses treatment. Meanwhile, the increase of the pulse number also promotes the superposition of the stress in the cooling and recrystallization process, and thus a greater surface plastic deformation formed. As presented in Fig. 6, the slip bands are much wider and longer with the increasing pulse number and almost cover the entire modified surface after 5000 pulses treatment. Fig. 9 also illustrates the formation of deformation twins and subboundaries in the modified layer after a treatment of 5000 pulses.

3.2. Modification of properties

3.2.1. Microhardness

The variations in the microstructure of AISI 304 stainless steel sample surface after PSPEB treatment have a significant effect on the mechanical properties. In this section, the surface microhardness of AISI 304 stainless steel samples before and after PSPEB treatment with varying pulses is investigated, and the results are shown in Fig. 11. The results reveal that the surface microhardness is increased with the number of pulses. Under 5000 pulses treatment, the surface microhardness is increased to 257 HV, which is a 40% increase compared with the untreated sample of 184 HV. Considering the microstructure evolution in the modified surface of the treated sample, the improvement of surface microhardness is mainly dependent on the gain refinement and the strengthening of plastic deformations of slip bands, dislocations and twins, which are all enhanced with the number of beam pulses inceased.

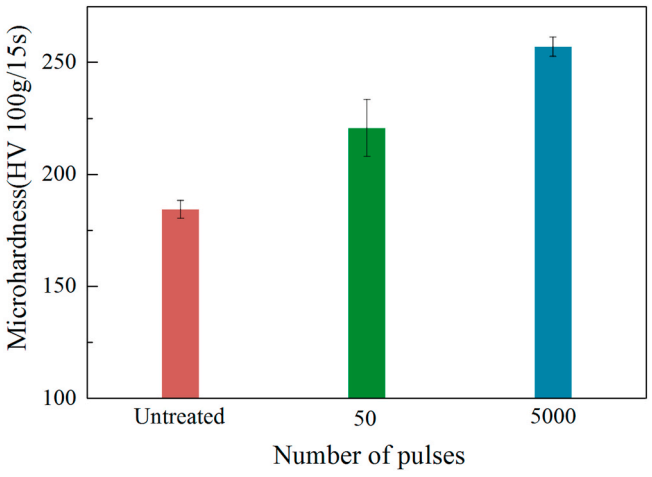

Fig. 11. Surface microhardness of AISI 304 stainless steel samples before and after PSPEB treatment under varying number of pulses.

3.2.2. Corrosion properties

The effect of PSPEB treatment on the corrosion resistance of AISI 304 stainless steel sample is evaluated by potentiodynamic polarization and electrochemical impendence spectrometry (EIS) tests as shown in Fig. 12.

Firstly, the polarization curves of AISI 304 stainless steel samples before and after treatment with varying pulse number measured from −0.6 to −0.1 V are presented in Fig. 12(a). Generally, the cathodic polarization curve mainly represents the cathodic hydrogen evolution, while the anodic one represents the dissolution of metal cation in the corrosion environment [43]. The corrosion potential E_{corr}, is measured to be −0.367 V vs SCE of the untreated sample. It is first increased to −0.365 V after 50 pulses treatment and then to −0.292 V after 5000 pulses treatment. With the number of pulses increased, the corrosion current density I_{corr}shows a fluctuation: it is first decreased from 4.281×10^{-5} A/cm^2 for the untreated sample to 2.917×10^{-6} A/cm^2 after 50 pulses treatment, then increased to 1.441×10^{-5} A/cm^2 after 5000 pulses treatment. It can be demonstrated that the corrosion resistance is effectively enhanced for the samples after PSPEB treatment with the corrosion potential increased while the corrosion current density decreased.

Secondly, the EIS analysis is implemented to investigate the electrochemical reaction mechanism of AISI 304 stainless steel samples before and after PSPEB treatment in the 5 wt% NaCl water solution. As shown in Fig. 12(b), the Nyquist plot of the untreated sample shows obviously curved capacitive loop compared with the treated ones, and the radius of the capacitive loop is increased with the pulse number. The radius of the capacitive loop represents the value of polarization resistance, and large radius is corresponding to the high resistance [44]. The variation of radius illustrates that the polarization resistance is increased with the pulse number. Furthermore, the value of polarization resistance after 5000 pulses treatment is increased by more than a half of magnitude compared with the untreated one. Fig. 12(c) displays the bode plots for resistance modulus |Z| versus frequency f. The resistance value at the high frequency region represents the solution resistance, while that at low frequency region is mainly attributed to the sum of solution resistance and polarization resistance [45–48]. The results reveal that in high frequency region, the values of solution resistance of samples after 50 pulses and 5000 pluses treatments are both higher than that of untreated sample as shown in the inset of Fig. 12(c), indicating that the surface condition of the treated sample is more stable, and less corrosion products enter into the corrosive solution. In the low frequency section, the polarization resistance of samples after 5000 pulses treatment is higher than that of the untreated sample, which is identical with the result in Nyquist plots in Fig. 12(b).

Furthermore, Fig. 13 gives the corrosion-damaged surface morphology of AISI 304 stainless steel sample surface under 50 pulses treatment. There are some pitting corrosion pits with diameter ranging from 10 μm to 50 μm. Most of large pits are generally located outside the modified zone center, indicating that the corrosion resistance of the modified zone center is better than the external region. Fig. 13(b) reveals that the micromorphology of the pitting corrosion pit is a typical lamellar structure.

In this work, the mechanism of improved corrosion potential of PSPEB irradiated samples is principally caused by the efficient elimination of the irradiated surface from Cr element segregation and undesirable carbon-containing inclusions. During the PSPEB irradiation process, the local concentration of Cr element and inclusions are greatly eliminated. Thus, the spots on the surface which are sensitive to corrosion are eliminated and the corrosion potential of pitting is improved obviously. Additionally, the homogeneous layer at the top surface formed by multiple PSPEB pulses with rapid heating and cooling processes results in less potential for the galvanic coupling [49]. The homogenization of alloying elements is favorable for reducing the formation of soluble chloride with the metal cation in the passive film,

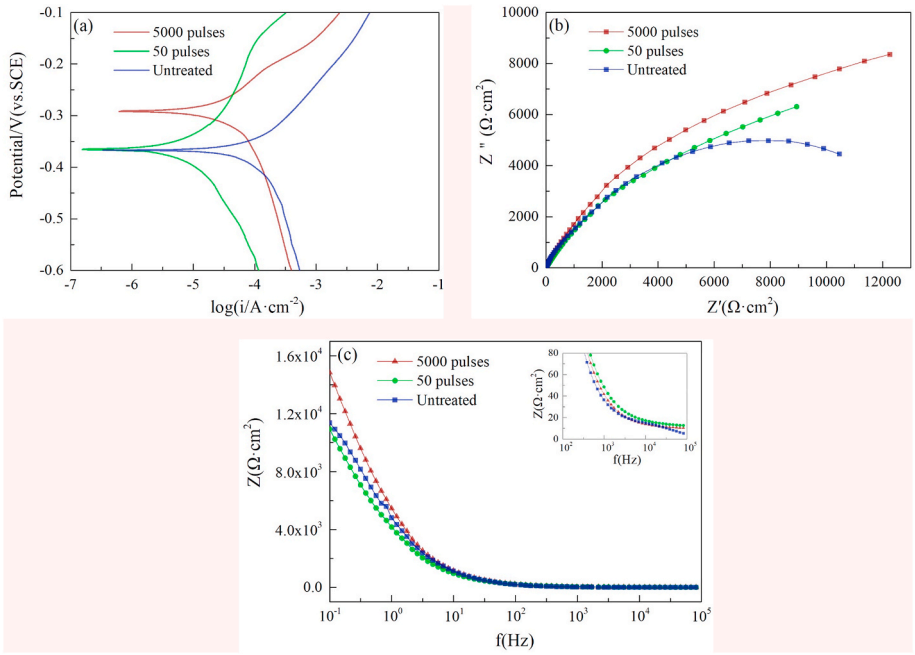

Fig. 12. Electrochemical test results of AISI 304 stainless steel samples before and after PSPEB treatment under varying number of pulses: (a) polarization curves; (b) Nyquist plots; (c) bode plots for modulus Z vs frequency f.

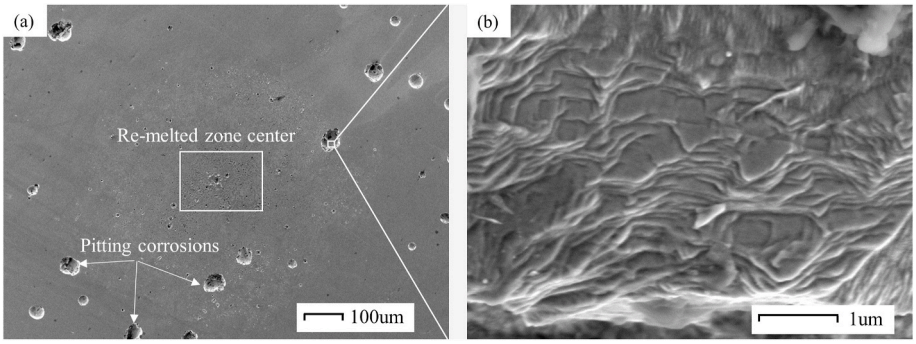

Fig. 13. Corrosion-damaged surface morphology under 50 pulses treatment.

and thus restricting the pitting formation and extension.

3.3. Effects of residual gas on the surface

In this experiment, the vacuum chamber is pumped by a molecular pump system to the pressure below10^{-3} Pa, and then argon is filled into the vacuum chamber for 50 min. Finally, the vacuum chamber is adjusted to the working pressure range of$4\tilde{}8 \times 10^{-1}$Pa, which is within the sub-vacuum range, and thus the effects of residual gas in vacuum chamber on the sample surface is investigated in this section.

3.3.1. Effects of the plasma ionized from residual argon

The residual argon in the electron beam transmission vacuum chamber is ionized by the high-energy electron beam, which creates a plasma area around the electron beam. This plasma then interacts with the material surface. The results of the plasma processing area in the

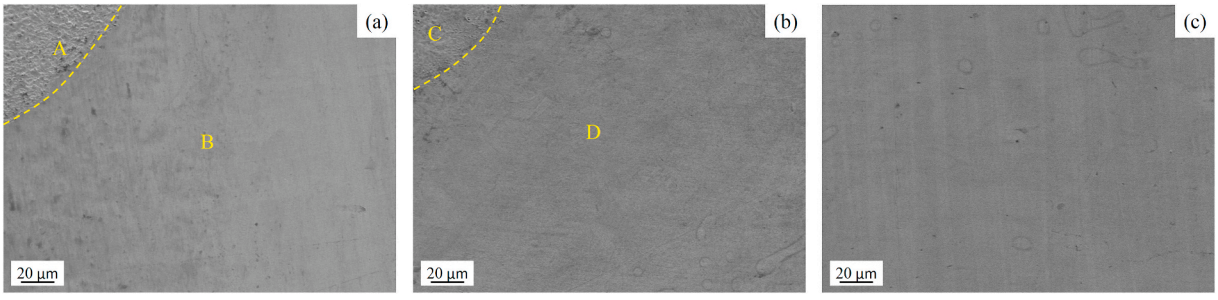

Fig. 14. SEM images of the plasma processing area of AISI 304 stainless steel sample surfaces after PSPEB treatment of: (a) 50 pulses; (b) 5000 pulses; (c) untreated sample.

surface observed by SEM are shown as follows. Fig. 14(a) and (b) present the treated samples by PSPEB under 50 and 5000 pulses, and Fig. 14(c) shows the untreated sample. The areas marked with "A" and "C" are the electron beam processing areas, and "B" and "D" are the plasma processing areas. It can be observed that the microstructure and micromorphology of the plasma treated area are similar to those of the untreated area, which is obviously different from the re-melting morphology of the electron beam treated area, indicating that the plasma generated by the ionization of residual argon has no obvious effect on the sample surface. An amount of energy loss in the process of plasma generation is mainly caused by the collisions and ionizations between the high energy electrons with the residual argon gas. Then the plasma energy is greatly decreased and its kinetic energy is also greatly decreased. Thus it can be assumed that under such a low energy range, the interactions between the plasma and the sample surface cannot produce significant microstructural variations.

3.3.2. *Residual gas contamination*

Considering the influence of the residual gas contamination, elemental mapping by EDS for oxygen and argon elements on the sample surface is performed. The measurement results are shown as follows. According to Fig. 15 and Table 3, the argon element content on the treated surface is almost zero, illustrating that the residual argon hardly contaminates the sample surface. The oxygen element content on the treated surface is approximately 3%. However, considering the content of carbon element on the standard AISI 304 stainless steel sample (0.08%) and that on the 5000 pluses treatment sample (approximately 5%), it can be demonstrated that the sample inevitably undergoes oxidation and organic contamination slightly during its removal from the vacuum chamber to the measurement system. Therefore, the oxygen element content (3%) is mainly caused by the oxidation and organic contamination outside the vacuum chamber, and the residual oxygen contamination in our vacuum environment can be negligible, which is also identical with the analysis presented in Ref. [50] that the secondary oxidation of the material surface can be avoided under the pulsed electron beam treatment in vacuum chamber.

4. Conclusions

In this work, the evolution of the microstructure and properties of AISI 304 stainless steel via a series processes of PSPEB treatment with varying number of pulses were investigated and analyzed. The main results were summarized as follows:

(1) After PSPEB treatment, a modified zone with thickness of 1–4 μm was formed on the irradiation samples, on which the crater was appeared. With the increase of the pulse number, the randomly dispersed crater morphology was removed, and the connected bulge and depression morphology was formed.
(2) With the increase of the pulse number, the break-up of the precipitated ferrite secondary phase and its subsequent dissolution greatly reduced the level of Cr alloying element segregation, promoting the formation of more homogenous composition in the modified layer.
(3) After 5000 pulses treatment, the homogenous submicron grains with slip bands in different directions were distributed fully in the modified layer completely replacing the original coarse grains (more than 10 μm). Simultaneously, the multiple abundant microstructures including dislocations, sub-boundaries and nanotwins with the twin lamella thickness no more than 8 nm were induced by PSPEB treatment in the modified layer.
(4) The PSPEB treated samples exhibited higher microhardness values, and the performances were improved with the increased pulse number. The improvement of surface microhardness was mainly attributed to the gain refinement and plastic deformation strengthening of slip bands, dislocations and twins.
(5) For the treated samples, the corrosion potential E_{corr} and polarization resistance both showed a rising trend, while the corrosion current density I_{corr} was decreased by nearly an order of magnitude, which illustrated that the corrosion resistance of the treated samples was improved obviously. The homogenization of alloying elements, especially the reduction of Cr segregation, and removal of the inclusions were jointly conductive to the improvement of corrosion resistance.
(6) In the sub-vacuum environment with operating pressure of $4\tilde{}8 \times 10^{-1}$ Pa, the plasma produced by the collisions and ionizations between the high energy electrons with the residual argon gas had no significant effect on the sample surface. There was also no contamination of residual gas on the sample surface.

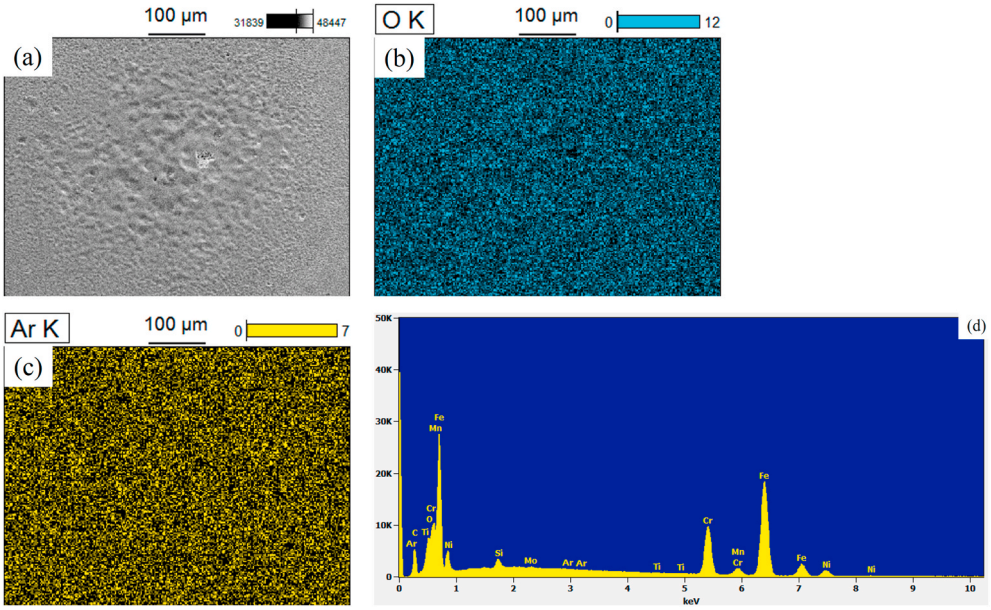

Fig. 15. Elemental mapping by EDS for oxygen and argon elements on the sample surface after 5000 pulses treatment.

Table 3
The element compositions measured by EDS mapping (wt%).

Element	Fe	Cr	Ni	C	O	Si	Mn	Mo	Ti	Ar
50 pulses	64.10	18.20	6.68	5.33	3.21	1.00	0.88	0.24	0.35	0.00
5000 pulses	64.68	18.67	6.50	5.10	3.07	1.05	0.61	0.23	0.07	0.02

Declaration of competing interest

The authors declare that they have no known competing financial interests or personal relationships that could have appeared to influence the work reported in this paper.

Acknowledgement

The authors gratefully acknowledge the financial support by Youth Program of National Natural Science Foundation of China (Grant No. 51505285).

References

[1] J. Beddoes, J.G. Parr, Effect of electropulsing on surface mechanical properties and Microstructure of AISI 304 stain less steel during ultrasonic surface rolling process, Mater. Sci. Eng. 662 (2016) 456–467.
[2] M.K. Lei, X.M. Zhu, In vitro corrosion resistance of plasma source ion nitrided austenitic stainless steels, Biomaterials 22 (2001) 641–647.
[3] E. Cakmak, S.C. Vogel, H. Choo, Effect of martensitic phase transformation on the hardening behavior and texture evolution in a AISI 304L stainless steel under compression at liquid nitrogen temperature, Mater. Sci. Eng. 589 (2014) 235–241.
[4] X.L. Lu, X.B. Liu, et al., Effects of heat treatment on microstructure and mechanical properties of Ni60/h-BN self-lubricating anti-wear composite coatings on AISI 304 stainless steel by laser cladding, Appl. Surf. Sci. 355 (2015) 350–358.
[5] J.D. Majumdar, Mechanical and electro-chemical properties of laser surface alloyed AISI 304 stainless steel with WC+Ni+NiCr, Phys. Procedia. 41 (2013) 335–345.
[6] G.P. Singh, J. Alphonsa, P.K. Barhai, et al., Effect of surface roughness on the properties of the layer formed on AISI 304 stainless steel after plasma nitriding, Surf. Coating. Technol. 200 (2006) 5807–5811.
[7] T. Hong, M. Nagumo, The effect of chloride concentration on early stages of pitting for type AISI 304 stainless steel revealed by the AC impedance method, Corrosion Sci. 39 (1997) 285–293.
[8] A.Y. Chen, H.H. Ruan, J. Wang, et al., The influence of strain rate on the microstructure transition of AISI 304 stainless steel, Acta Mater. 59 (2011) 3697–3709.
[9] A.A. Abbasi, M. Zakeri, M.H. Moayed, et al., Effect of grain size on pitting corrosion of AISI 304L austenitic stainless steel, Corrosion Sci. 94 (2015) 368–376.
[10] Z. Zhang, J. Cai, L. Ji, et al., Microstructures and corrosion mechanism of AISI 304L stainless steel irradiated by high current pulsed electron beam, Protect. Met. Phys. Chem. Surface 50 (2014) 650–658.
[11] D.I. Proskurovsky, V.P. Rotshtein, G.E. Ozur, et al., Pulsed electron-beam technology for surface modification of metallic materials, J. Vac. Sci. Technol. 16 (1998) 2480–2488.
[12] P. Petrov, et al., Study of the influence of electron beam treatment of Ti5Al4V substrate on the mechanical properties and surface topography of multilayer TiN/TiO2 coatings, Vacuum 154 (2018) 264–271.
[13] D. Luo, G. Tang, X. Ma, et al., The microstructure of Ta alloying layer on M50 steel after surface alloying treatment induced by high current pulsed electron beam, Vacuum 136 (2017) 121–128.
[14] M. Iqbal, I. Shaukat, A. Mahmood, et al., Surface modification of mild steel with Boron Carbide reinforcement by electron beam melting, Vacuum 85 (2010) 45–47.
[15] K. Weigel, K. Bewilogua, M. Keunecke, et al., Effects of electron beam treatment on Ti(1-x)AlxN coatings on steel, Vacuum 107 (2014) 141–144.
[16] J. Lu, D.Q. Wei, R. Wang, et al., Surface polishing and modification of 3Cr2Mo mold steel by electron beam irradiation, Vacuum 143 (2017) 283–287.
[17] D.I. Proskurovsky, V.P. Rotshtein, G.E. Ozur, Use of low-energy, high-current electron beams for surface treatment of materials, Surf. Coating. Technol. 96 (1997) 117–122.
[18] Y. Uno, A. Okada, K. Uemura, et al., A new polishing method of metal mold with large-area electron beam irradiation, J. Mater. Process. Technol. 187 (2007) 77–80.
[19] J. Kim, J.S. Kim, E.G. Kang, et al., Surface modification of the metal plates using continuous electron beam process (CEBP), Appl. Surf. Sci. 311 (2014) 201–207.
[20] H.W. Park, I. Lee, Large pulsed electron beam surface treatment of translucent PMMA, Appl. Surf. Sci. 308 (2014) 311–315.
[21] D.Q. Wei, X.B. Wang, R. Wang, et al., Surface modification of 5CrMnMo steel with continuous scanning electron beam process, Vacuum 149 (2018) 118–123.
[22] S.O. Cetiner, P. Stoltz, et al., Dependence of electron peak current on hollow cathode dimensions and seed electron energy in a pseudospark discharge, J. Appl. Phys. 103 (2008) 304, 023AISI.
[23] R. Tkotz, A. Gortler, J. Christiansen, et al., Pseudospark switches-technological aspects and application, IEEE Trans. Plasma Sci. 23 (1995) 309–317.
[24] N. Kumar, P.U. Narayan, et al., Experimental investigation of a 1 kA/cm2 sheet beam plasma cathode electron gun, Rev. Sci. Instrum. 86 (2015), 013503.
[25] E. Dewald, K. Frank, D.H.H. Hoffmann, et al., Pulsed intense electron beams generated in transient hollow cathode discharges: fundamentals and applications, IEEE Trans. Plasma Sci. 25 (1997) 272–278.
[26] H. Jing, Y.L. Fu, et al., Hybrid particle-thermodynamic model and experimental validation of multi-track periodical heating during electron beam treatment, Nucl. Instrum. Methods B. 439 (2019) 34–42.
[27] T. Grosdidier, J.X. Zou, B. Bolle, et al., Grain refinement, hardening and metastable phase formation by high current pulsed electron beam (HCPEB) treatment under heating and melting modes, J. Alloys Compd. 504 (2010) 508–511.
[28] S. Hao, P. Wu, J. Zou, et al., Microstructure evolution occurring in the modified surface of 316L stainless steel under high current pulsed electron beam treatment, Appl. Surf. Sci. 253 (2007) 5349–5354.
[29] K.M. Zhang, J.X. Zou, T. Grosdidier, Crater-formation-induced metastable structure in an AISI D2 steel treated with a pulsed electron beam, Vacuum 86 (2012) 1273–1277.
[30] K.M. Zhang, J.X. Zou, T. Grosdidier, et al., Improved pitting corrosion resistance of AISI 316L stainless steel treated by high current pulsed electron beam, Surf. Coating. Technol. 201 (2006) 1393–1400.
[31] J.X. Zou, T. Grosdidier, C. Dong, Mechanisms of nanostructure and metastable phase formations in the surface melted layers of a HCPEB-treated D2 steel, Acta Mater. 54 (2006) 5409–5419.
[32] C.L. Zhang, P. Lv, H.D. Xia, et al., The microstructure and properties of nanostructured Cr-Al alloying layer fabricated by high-current pulsed electron beam, Vacuum 167 (2019) 263–270.
[33] S. Hao, H. Wang, L. Zhao, Surface modification of 40CrNiMo7 steel with high current pulsed electron beam treatment, Nucl. Instrum. Methods B. 368 (2016) 81–85.
[34] Q.F. Guan, H. Zou, G.T. Zou, et al., Surface nanostructure and amorphous state of a low carbon steel induced by high-current pulsed electron beam, Surf. Coating. Technol. 196 (2005) 145–149.
[35] K.M. Zhang, X. Jin, et al., Surface microstructure and property modifications in a duplex stainless steel induced by high current pulsed electron beam treatments, J. Alloys Compd. 707 (2017) 178–183.
[36] X. Zhang, K.M. Zhang, J.X. Zou, et al., Surface microstructure modifications and in-vitro corrosion resistance improvement of a WE43 Mg alloy treated by pulsed electron beams, Vacuum 173 (2020), 109132.
[37] J. Zhang, J. Zhao, Characteristics of plasma based on electron beams produced in pseudospark discharge under nanosecond pulsed voltages, IEEE Trans. Plasma Sci. 42 (2014) 2824–2825.
[38] J.M. Xiao, Metallic Problems of High Speed Steel, Metallurgical Industry Press, Beijing, 1978.
[39] K.M. Zhang, J.X. Zou, B. Bolle, et al., Evolution of residual stress states in surface layers of an AISI D2 steel treated by low energy high current pulsed electron beam, Vacuum 87 (2013) 60–68.
[40] Y.R. Liu, K.M. Zhang, J.X. Zou, et al., Effect of the high current pulsed electron beam treatment on the surface microstructure and corrosion resistance of a Mg-4Sm alloy, J. Alloys Compd. 741 (2018) 65–75.
[41] S. Hao, X. Zhang, X. Mei, T. Grosdidier, C. Dong, Surface treatment of DZ4 directionally solidified nickel-based superalloy by high current pulsed electron beam, Mater. Lett. 62 (2008) 414–417.
[42] C.L. Zhang, N.N. Tian, L. Li, et al., The effect of high-current pulsed electron beam on phase formation and surface properties of chromium/copper system, Vacuum 174 (2020), 109222.
[43] G.L. Song, Z.Q. Xu, The surface, microstructure and corrosion of magnesium alloy AZ31 sheet, Electrochim. Acta 55 (2010) 4148–4161.
[44] C. Liang, L. Liu, Z. Jia, C. Dai, Y. Xiong, Synergy of Nyquist and Bode electrochemical impedance spectroscopy studies to particle size effect on the electrochemical properties of LiNi0.5Co0.2Mn0.3O2, Electrochim. Acta 186 (2015) 413–419.
[45] C. Liang, L. Liu, Z. Jia, C. Dai, Y. Xiong, Synergy of Nyquist and Bode electrochemical impedance spectroscopy studies to particle size effect on the electrochemical properties of $LiNi_{0.5}Co_{0.2}Mn_{0.3}O_2$, Electrochim. Acta 186 (2015) 413–419.
[46] G. Song, A. Atrens, D.S. John, X. Wu, J. Nairn, The anodic dissolution of magnesium in chloride and sulphate solutions, Corrosion Sci. 39 (1997) 1981–2004.
[47] F.L. Floyd, S. Avudaiappan, J. Gibson, B. Mehta, P. Smith, T. Provder, J. Escarsega, Using electrochemical impedance spectroscopy to predict the corrosion resistance of unexposed coated metal panels, Prog. Org. Coating 66 (2009) 8–34.

[48] A. Nishikata, Y. Ichihara, T. Tsuru, An application of electrochemical impedance spectroscopy to atmospheric corrosion study, Corrosion Sci. 37 (1995) 897–911.
[49] Y. Samih, G. Marcos, N. Stein, N. Allain, E. Fleury, C. Dong, T. Grosdidier, Microstructure modifications and associated hardness and corrosion improvements in the AISI 420 martensitic stainless steel treated by high current pulsed electron beam (HCPEB), Surf. Coating. Technol. 259 (2014) 737–745.
[50] X. Zhang, K.M. Zhang, J.X. Zou, et al., Surface microstructure modifications and in-vitro corrosion resistance improvement of a WE43 Mg alloy treated by pulsed electron beams, Vacuum 173 (2020), 109132.